

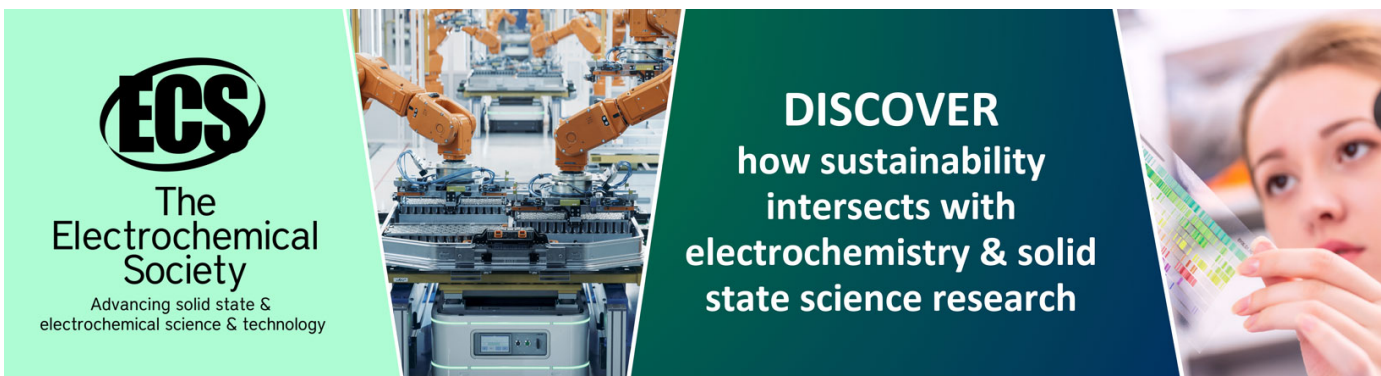
Vibration energy harvesting by magnetostrictive material

To cite this article: Lei Wang and F G Yuan 2008 *Smart Mater. Struct.* **17** 045009

View the [article online](#) for updates and enhancements.

You may also like

- [Kinetic and thermal energy harvesters for implantable medical devices and biomedical autonomous sensors](#)
Andrea Cadei, Alessandro Dionisi, Emilio Sardini et al.
- [Fabrication of PZT MEMS energy harvester based on silicon and stainless-steel substrates utilizing an aerosol deposition method](#)
Shun-Chiu Lin and Wen-Jong Wu
- [Electrostatic vibration energy harvester with combined effect of electrical nonlinearities and mechanical impact](#)
P Basset, D Galayko, F Cottone et al.



ECS
The
Electrochemical
Society
Advancing solid state &
electrochemical science & technology

DISCOVER
how sustainability
intersects with
electrochemistry & solid
state science research

Vibration energy harvesting by magnetostrictive material

Lei Wang and F G Yuan¹

Department of Mechanical and Aerospace Engineering, North Carolina State University, Raleigh, NC 27695-7921, USA

E-mail: yuan@ncsu.edu

Received 8 September 2007, in final form 19 March 2008

Published 3 June 2008

Online at stacks.iop.org/SMS/17/045009

Abstract

A new class of vibration energy harvester based on magnetostrictive material (MsM), Metglas 2605SC, is designed, developed and tested. It contains two submodules: an MsM harvesting device and an energy harvesting circuit. Compared to piezoelectric materials, the Metglas 2605SC offers advantages including higher energy conversion efficiency, longer life cycles, lack of depolarization and higher flexibility to survive in strong ambient vibrations. To enhance the energy conversion efficiency and alleviate the need of a bias magnetic field, Metglas ribbons are transversely annealed by a strong magnetic field along their width direction. To analyze the MsM harvesting device a generalized electromechanical circuit model is derived from Hamilton's principle in conjunction with the normal mode superposition method based on Euler–Bernoulli beam theory. The MsM harvesting device is equivalent to an electromechanical gyrator in series with an inductor. In addition, the proposed model can be readily extended to a more practical case of a cantilever beam element with a tip mass. The energy harvesting circuit, which interfaces with a wireless sensor and accumulates the harvested energy into an ultracapacitor, is designed on a printed circuit board (PCB) with plane dimension $25\text{ mm} \times 35\text{ mm}$. It mainly consists of a voltage quadrupler, a 3 F ultracapacitor and a smart regulator. The output DC voltage from the PCB can be adjusted within 2.0–5.5 V. In experiments, the maximum output power and power density on the resistor can reach $200\text{ }\mu\text{W}$ and $900\text{ }\mu\text{W cm}^{-3}$, respectively, at a low frequency of 58 Hz. For a working prototype under a vibration with resonance frequency of 1.1 kHz and peak acceleration of 8.06 m s^{-2} (0.82 g), the average power and power density during charging the ultracapacitor can achieve $576\text{ }\mu\text{W}$ and $606\text{ }\mu\text{W cm}^{-3}$, respectively, which compete favorably with piezoelectric vibration energy harvesters.

(Some figures in this article are in colour only in the electronic version)

1. Introduction

Wireless sensor networks (WSN) consisting of spatially distributed autonomous sensors have been increasingly deployed to access the health status of structures. The advantages of WSN over wired sensors include the ability of sensor communication, ease of network scalability, reducing the maintenance labor and cost, and increasing deployability of the sensors under a wide range of physical and environmental conditions. The lack of cables for power transmission, however, induces a constraint on power supply for each

individual sensor. The limited time-span of batteries is one of the greatest constraints on the longevity of WSN and inapplicable in long-term unattended monitoring. As a dense WSN is employed, replacing batteries becomes a time-consuming task which is ironically contradictory to the original objective of structural health monitoring (SHM). Besides, the bulky dimensions adds another limitation to battery-operated sensors.

A promising approach to circumvent these constraints is to integrate energy harvesting techniques with the wireless sensor to form a self-powered sensor node [1]. At present the harvested power is still much smaller than from batteries, but

¹ Author to whom any correspondence should be addressed.

Table 1. Summary of the comparison of the different vibrational types of harvesting mechanisms.

| Type | Advantages | Disadvantages |
|------------------|--|---|
| Electromagnetic | <ul style="list-style-type: none"> - no need of smart material - no external voltage source | <ul style="list-style-type: none"> - bulky size: magnets and pick-up coil - difficult to integrate with MEMS - max. voltage of 0.1 V |
| Electrostatic | <ul style="list-style-type: none"> - no need of smart material - compatible with MEMS - voltages of 2–10 V | <ul style="list-style-type: none"> - external voltage (or charge) source - mechanical constraints needed - capacitive |
| Piezoelectric | <ul style="list-style-type: none"> - no external voltage source - high voltages of 2–10 V - compact configuration - compatible with MEMS - high coupling in single crystals | <ul style="list-style-type: none"> - depolarization - brittleness in bulk piezolayer - poor coupling in piezo-film (PVDF) - charge leakage - high output impedance |
| Magnetostrictive | <ul style="list-style-type: none"> - ultra-high coupling coefficient >0.9 - no depolarization problem - high flexibility - suited to high frequency vibration | <ul style="list-style-type: none"> - nonlinear effect - pick-up coil - may need bias magnets - difficult to integrate with MEMS |

recent advances in integrated circuit (IC) manufacture, lower power CMOS circuitry and VLSI (very large scale integration) design have reduced the power consumption remarkably of commercial wireless sensors to the order of several to tens of mW and duty cycle to 1%. This trend enhances the feasibility of energy harvesting for WSN. Generally, electromagnetic, electrostatic and piezoelectric (PZT) are the three common vibration energy harvesting mechanisms [2–4] and table 1 compares the features of different vibration energy harvesting mechanisms. Currently, PZT is the most prevalent material because of its compact configuration and compatibility with MEMS (micro-electromechanical systems), but its inherent limitations, including aging, depolarization and brittleness, confine further applications in actual WSN [1, 4].

To overcome such limitations, a few attempts have been made to harvest ambient vibrations based on the *Villari effect*, that is, vibration-induced strain of an MsM produces a change in its magnetization [5]. Although most ferromagnetic materials exhibit the Villari effect, the low magnitude makes the materials impractical to be used. Two commercial giant MsMs have prompted a fresh look at energy harvesting applications: crystalline alloy Terfenol-D ($\text{Tb}_{0.3}\text{Dy}_{0.7}\text{Fe}_{1.9-2}$) [5] and amorphous metallic glass Metglas 2605SC ($\text{Fe}_{81}\text{B}_{13.5}\text{Si}_{3.5}\text{C}_2$) [6]. A Terfenol-D-based harvester could not be suitable for actual WSN [7]. Apart from its bulky dimensions containing two thousand-turned coils, its maximum output power was up to $45 \mu\text{W}$ at a resonant frequency of 45 Hz, and the peak AC output voltage was less than 0.35 V, which was lower than the forward voltage drop of diodes (0.2–0.4 V at 1 mA), let alone for voltage rectification.

Due to the giant magnetostriction of Terfenol-D up to 2000μ , Terfenol-D has been used as a medium to provide large extensional strains in a PZT layer for energy harvesting. A thin PZT layer sandwiched by two Terfenol-D layers is placed under a time-varying magnetic field. Since the outer Terfenol-D layers will induce higher strains than the traditional d_{31} bending mode in the PZT layer, the PZT layer will generate more charge. The time-varying magnetic field could be induced from ambient vibrations by a permanent

magnet attached to either a cantilever beam or a spring [8, 9]. The hybrid approach could be an alternative scheme for PZT-based energy harvesting, but two coupling mechanisms and load transfer between interlayers would further reduce the conversion efficiency; this approach is still facing the similar limitations of PZT-based harvesters. To the authors' best knowledge, the thin-film giant amorphous Metglas has been routinely employed as power transformers and current transducers [6]; however, its ultra-high magnetomechanical coupling for energy conversion has not been employed for energy harvesting.

The purpose of this paper is to develop a new class of energy harvesting scheme based on amorphous Metglas 2605SC. A prototype design for the MsM harvester is proposed and a general architecture for energy-harvesting-based sensor nodes is discussed. Because the Metglas can be annealed under a strong transverse magnetic field in its width direction, this treatment not only enhances the magnetomechanical coupling coefficient $k > 0.9$ [10, 11] but also mitigates the need for a bias magnetic field, further reducing the dimension of the harvester. To predict the output performance, governing equations are derived from Hamilton's principle in conjunction with the normal mode superposition method based on Euler–Bernoulli beam theory. Meanwhile, the output performance of the MsM harvesting device powering a resistive load and charging a capacitive storage device, respectively, has been analyzed. A compact PCB consists of a voltage quadrupler, a 3 F ultracapacitor and a smart regulator. Compared to chemical rechargeable batteries, ultracapacitors can achieve instant charging, about 10 times higher charge/discharge efficiency, semi-permanent life cycles, lower cost and smaller footprint (1/7 of AA batteries) [12]. The output DC voltage from the PCB can be adjusted within 2.0–5.5 V. In experiments, the output power and power density on the resistive load and the ultracapacitor are investigated under low and high frequencies, respectively, which compete favorably with piezoelectric vibration energy harvesters. Finally the challenges of current design and future work are discussed.

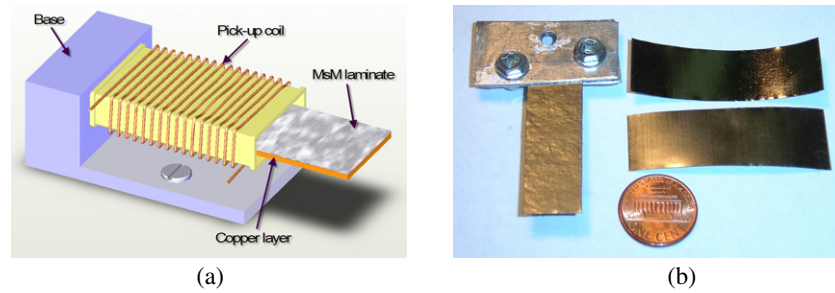


Figure 1. (a) Prototype of the MsM energy harvesting device, (b) MsM layer (Metglas 2065SC) and laminate.

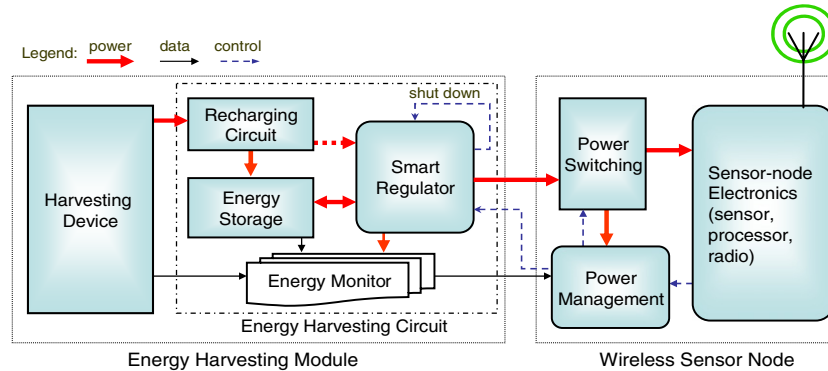


Figure 2. General framework of an energy harvesting module and compatible wireless sensor nodes.

2. Prototype of the MsM vibration energy harvester

The new MsM vibration energy harvester has two units: a harvesting device comprising a giant MsM (Metglas 2605SC) bonded on a copper substrate wound by a pick-up coil as shown in figure 1(a), and an energy harvesting circuit discussed in section 4. Due to the thin thickness ($18\ \mu\text{m}$) of the standard Metglas 2605SC ribbon, several MsM ribbons are laminated as shown in figure 1(b) to enhance energy harvesting capability. The MsM laminate utilizes the Villari or sensing effect of magnetostriction, where vibration-induced strains caused by bending produce a change in the magnetization of the MsM laminate. Upon dynamic or cyclic loading, this change in magnetization is converted into electrical energy using a pick-up coil surrounding the MsM laminate according to Faraday's law. One drawback of the other giant MsM, Terfenol-D, for energy harvesting is the requirement for a bias magnetic field and this leads to bulky dimensions. In this study, a strong transverse magnetic field is introduced to anneal Metglas such that it could mitigate the usage of a bias magnetic field and reduce the harvester's footprint [10, 11].

In contrast to battery-powered sensors, power availability in energy-harvesting-based sensors varies in time and may vary at different sensor nodes in the network. Therefore, energy-harvesting-based wireless sensors need additional modules to interface with the harvester and manage the harvested energy. As proposed in figure 2, the energy-harvesting-based wireless sensor has a complicated architecture including an energy harvesting module with two built-in units: a harvesting device and an energy harvesting circuit. Note that this generic

architecture is not only suitable for MsM, but also applicable for other types of harvesting techniques.

The *harvesting device* generates usable electrical energy from the environment. It can be implemented by two mechanisms: one is based on materials for energy conversion such as piezoelectric material, thermocouple, solar cell, etc; the other relies on structures for energy conversion such as electromagnetic harvesters and electrostatic harvesters.

Rechargeable batteries and ultracapacitors are commonly used as *energy storage devices*. The *recharging circuit* is a condition circuit for the energy storage device and has at least two functions. One is rectification, converting AC to DC voltage implemented by a diode bridge. An essential premise of the rectification is that the amplitude of the AC output voltage from the harvesting device must be higher than the forward voltage drop of the diodes. The other function is to match the charging profile of the energy storage device. For instance, a rechargeable battery must be charged by a voltage greater than its output, and an ultracapacitor may be inoperative if the charging voltage exceeds its rated voltage.

The *smart regulator* resembles a smart valve adjusting the output power from the harvester module to drive the wireless sensor node. In addition to voltage regulation, it can self-shutdown when the energy storage device cannot afford the consumption of the wireless sensor. To enhance the energy utilization, the smart regulator can bypass the energy storage device and directly connect to the recharging circuit as long as the amount of power is sufficient to drive the wireless sensors. Furthermore, the performance of the smart regulator can be optimized through adjusting output voltage or current

by a control signal from a power management component. The *energy monitor* tracks the available energy from the environment, as well as the state of the energy storage device. Such data will be fed into the power management algorithms for learning the energy environment. A voltage follower with low power consumption is suited for implementation.

Apart from the usual wireless sensor electronics, two new submodules, referred to as *power switching* and *power management*, need to be integrated with the wireless sensor for establishing a compatible interface with the energy harvester circuit board. The power from the harvester board, which is controlled by the power switching, drives all the electronics of the wireless sensor board. This submodule is useful for turning on or off various components as the amount of environmental availability varies. The *power management* submodule is a unique and essential component for at least two reasons. First, the environmental energy source highly varies. Unlike a battery supply, which is simply characterized by the amount of residual energy and reliably available, the characterization of environmental energy is time-dependent and more complicated. Second, the environmental energy has the potential to be used permanently. The energy monitor records the characterization of the environmental energy and sends to the power management submodule. It may be integrated as a part of the built-in sensor processor and preloaded with a power management algorithm.

3. Theoretical modeling

3.1. Constitutive equations of MsM

The magnetic and mechanical behavior of magnetostriction with neglect of thermal effects is given in the tensor expression [5]

$$\varepsilon_{ij} = s_{ijkl}^H \sigma_{kl} + d_{kij} H_k + m_{klj} H_k H_l \quad (1a)$$

$$B_j = d_{jkl}^* \sigma_{kl} + \mu_{jk}^T H_k \quad (1b)$$

where ε and σ are mechanical strain and stress, respectively, H and B are magnetic field intensity and flux density, respectively, s^H is the elastic compliance under constant magnetic field and μ^T is the permeability under constant stress.

The above nonlinear constitutive equations in one dimension can be linearized using two equations that are similar to the equations for linearized uniaxial piezoelectric materials [13]:

$$\begin{Bmatrix} \varepsilon \\ B \end{Bmatrix} = \begin{bmatrix} s^H & d \\ d^* & \mu^T \end{bmatrix} \begin{Bmatrix} \sigma \\ H \end{Bmatrix} \quad (2)$$

where the two magnetomechanical coefficients are defined experimentally by the following two equations:

$$d = \left. \frac{\partial \varepsilon}{\partial H} \right|_{\sigma}, \quad d^* = \left. \frac{\partial B}{\partial \sigma} \right|_H \quad (3)$$

where subscripts σ and H refer to measurements at constant stress and constant applied magnetic field, respectively. For small strains, d and d^* can be considered to be equal.

The constitutive equation (2) can be rearranged as [13]

$$\begin{Bmatrix} \sigma \\ B \end{Bmatrix} = \begin{bmatrix} E^H & -e \\ e^* & \mu^S \end{bmatrix} \begin{Bmatrix} \varepsilon \\ H \end{Bmatrix} \quad (4)$$

where E^H is the Young's modulus of the MsM under constant magnetic field, μ^S is the permeability under constant strain, and constants e and e^* are defined as

$$e = E^H d, \quad e^* = E^H d^*. \quad (5)$$

Based on the usual convention in magnetostrictive materials [5, 14], axes 3 and 1 are in the length and width direction of the laminate, respectively. When the material is bent in the 2 axis, both induced axial strain and magnetization are in the 3 axis. Accordingly, the Metglas laminate operates in '33' mode. In the following, the subscript 33 is omitted [5, 15].

Assuming a linearized relationship between B , H , ε , and σ , the internal energy is given by

$$\mathcal{E} = \frac{1}{2} \varepsilon \sigma + \frac{1}{2} H B. \quad (6)$$

Substitution of ε and B into equation (6) by equation (2) yields

$$\begin{aligned} \mathcal{E} &= \frac{1}{2} \sigma s^H \sigma + \frac{1}{2} \sigma d H + \frac{1}{2} H d^* \sigma + \frac{1}{2} H \mu^T H \\ &= \mathcal{E}_m + \mathcal{E}_{mM} + \mathcal{E}_{Mm} + \mathcal{E}_M = \mathcal{E}_m + 2\mathcal{E}_{mM} + \mathcal{E}_M \end{aligned} \quad (7)$$

where subscripts m, M and mM (or Mm) indicate the mechanical, magnetic and mutual magnetoelastic energy, respectively.

An important figure of merit for MsM is the material coupling coefficient, k , which is defined as the ratio of the mutual magnetoelastic energy to the geometric mean of the mechanical and magnetic energy [5, 15]:

$$k = \frac{\mathcal{E}_{mM}}{\sqrt{\mathcal{E}_m \mathcal{E}_M}} = \frac{d}{\sqrt{\mu^T s^H}}. \quad (8)$$

3.2. Governing equations of the harvesting device

The constitutive equation (2) should be extended to model macro-behavior of the MsM harvesting device with an MsM unimorph and a pick-up coil. The MsM laminate bonded on a copper substrate forms a unimorph structure, as shown in figure 3(a) with x and z in the horizontal and vertical directions, respectively. Assume both copper substrate and Metglas laminate have the same width b and length l . An equivalent 1-DOF mass-spring-damper approximation model as shown in figure 3(b) was derived based on average strain [1]. However, this model is only valid in a frequency range up to the fundamental natural frequency. Since the MsM harvesting device may vibrate at higher frequencies, rigorous models need to be investigated.

The equations of motion can be derived from Hamilton's principle that all variations vanish over any time interval from t_1 to t_2 :

$$\int_{t_1}^{t_2} [\delta(T - U + W_M) + \delta W] dt = 0 \quad (9)$$

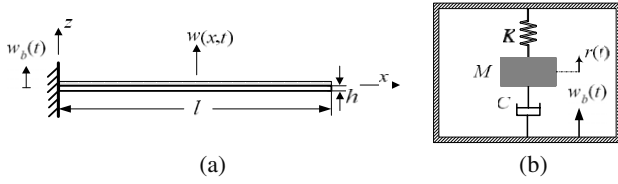


Figure 3. (a) Geometry of the beam element in side view, (b) equivalent 1-DOF mass-spring-damper element model obtained by modal projection.

where the kinetic energy T , strain energy U and magnetic energy W_M are defined as

$$T = \frac{1}{2} \int_{V_s} \rho_s \dot{\mathbf{u}}^T \dot{\mathbf{u}} dV_s + \frac{1}{2} \int_{V_M} \rho_M \dot{\mathbf{u}}^T \dot{\mathbf{u}} dV_M \quad (10a)$$

$$U = \frac{1}{2} \int_{V_s} \boldsymbol{\varepsilon}^T \boldsymbol{\sigma} dV_s + \frac{1}{2} \int_{V_M} \boldsymbol{\varepsilon}^T \boldsymbol{\sigma} dV_M \quad (10b)$$

$$W_M = \frac{1}{2} \int_{V_M} B H dV_M \quad (10c)$$

where the dot indicates time derivative, superscript T denotes transpose operation, and subscripts s and M indicate the copper substrate and MsM layer, respectively. The mechanical displacement is $\mathbf{u}(x, t)$, and ρ is the mass density. Since equation (9) does not include electrical energy on an external electrical load, the formulation here is in short-circuit condition for the pick-up coil.

The external work W , caused by N_f discretely applied external point forces $\mathbf{f}_k(t)$ at positions x_k , is given by

$$\delta W = \sum_{k=1}^{N_f} \delta \mathbf{u}_k \mathbf{f}_k(t). \quad (11)$$

With consideration of the above definitions and the constitutive relations of equations (4), (9) is rewritten as

$$\begin{aligned} & \int_{t_1}^{t_2} \left[\int_{V_s} \rho_s \delta \dot{\mathbf{u}}^T \dot{\mathbf{u}} dV_s + \int_{V_M} \rho_M \delta \dot{\mathbf{u}}^T \dot{\mathbf{u}} dV_M - \int_{V_s} E_s \delta \boldsymbol{\varepsilon}^T \boldsymbol{\varepsilon} dV_s \right. \\ & - \int_{V_M} E^H \delta \boldsymbol{\varepsilon}^T \boldsymbol{\varepsilon} dV_M + \int_{V_M} e \delta \boldsymbol{\varepsilon}^T H dV_M \\ & + \int_{V_M} e^* \delta H \boldsymbol{\varepsilon} dV_M + \int_{V_M} \mu^S \delta H H dV_M \\ & \left. + \sum_{k=1}^{N_f} \delta \mathbf{u}_k \mathbf{f}_k(t) \right] dt = 0 \end{aligned} \quad (12)$$

where E_s is the Young's modulus of the copper substrate.

In order to deduce the equations of motion from equation (12), some assumptions are made. The first assumption follows the Rayleigh–Ritz procedure, which states the displacement of a structure can be expressed as the superposition of N_r individual modes $\phi_i(x)$, multiplied by a generalized coordinate $r_i(t)$ [16, 17]. Second, only the transverse displacement is considered and the mode shape $\phi_i(x)$ is a function of $x \in [0, l]$, such that $\mathbf{u}(x, t) = (0, 0, w(x, t))$. Third, the base excitation is assumed to be only

in the transverse direction. The last assumption is to apply the Euler–Bernoulli beam theory for the axial strain ε :

$$w(x, t) = \sum_{r=1}^{N_r} \phi_r(x) r_r(t) = \boldsymbol{\phi}(x) \mathbf{r}(t) \quad (13)$$

$$\varepsilon = -z \frac{\partial^2 w(x, t)}{\partial x^2} = -z \boldsymbol{\phi}''(x) \mathbf{r}(t) \quad (14)$$

where $\boldsymbol{\phi} = [\phi_1(x), \dots, \phi_{N_r}(x)]$ is the modal vector, $\mathbf{r}(t) = [r_1(t), \dots, r_{N_r}(t)]^T$ is the generalized coordinate vector and the prime indicates the derivative to the axial position x .

With an assumption of long solenoid coil and neglecting fringing effects, magnetic field intensity H can be expressed by Ampère's law:

$$H = Ni/l \quad (15)$$

where N is the number of turns of the pick-up coil and i is the induced current.

The above assumptions can simplify equation (12) in terms of modal matrices to obtain the equations of motion as follows:

$$\mathbf{M} \ddot{\mathbf{r}} + \mathbf{K} \mathbf{r} + \mathbf{G} \mathbf{i} = \sum_{k=1}^{N_f} \boldsymbol{\phi}^T(x_k) f_k(t) \quad (16a)$$

$$\mathbf{G}^T \mathbf{r} - L \mathbf{i} = 0 \quad (16b)$$

where modal parameters are given, respectively, by

$$\mathbf{M} = \int_{V_s} \rho_s \boldsymbol{\phi}^T(x) \boldsymbol{\phi}(x) dV_s + \int_{V_M} \rho_M \boldsymbol{\phi}^T(x) \boldsymbol{\phi}(x) dV_M \quad (17a)$$

$$\mathbf{K} = \int_{V_s} E_s \boldsymbol{\phi}^{'T}(x) \boldsymbol{\phi}''(x) z^2 dV_s + \int_{V_M} E^H \boldsymbol{\phi}^{'T}(x) \boldsymbol{\phi}''(x) z^2 dV_M \quad (17b)$$

$$\mathbf{G} = \frac{Nd^* E^H A_M h_M}{l} \int_0^l \boldsymbol{\phi}^{'T}(x) dx \quad (17c)$$

$$L = \frac{\mu^S N^2 A_M}{l} \quad (17d)$$

where $A_M = bt_M$ is the cross-sectional area of the Metglas laminate, h_M is the distance from the centroid of the Metglas laminate to the neutral axis and L is the equivalent inductor associated with the coil wound around the Metglas laminate. Note that \mathbf{G} is a function of mode shapes, but the inductor L is not.

The cantilever beam is discretized into N_f elements of length $(\Delta x)_{N_f}$ and the local inertial load is applied on the k th element, or $f_k = -m_k(\Delta x)_k \ddot{w}_B$, where m_k is the element mass per length and w_B is the known base displacement. With the limit of $(\Delta x)_k \rightarrow dx$, the summation reduces to the integral over the beam length. For simplicity it has been assumed that the beam is uniform in the axial direction such that $m(x) = m = \text{const}$. Substitution of the forcing function into the right-hand side of equation (16a) yields a so-called modal forcing vector \mathbf{F} [18]:

$$\mathbf{F} = \sum_{k=1}^{N_f} \boldsymbol{\phi}^T(x_k) f_k(t) = -m \ddot{w}_B \int_0^l \boldsymbol{\phi}^T(x) dx \quad (18)$$

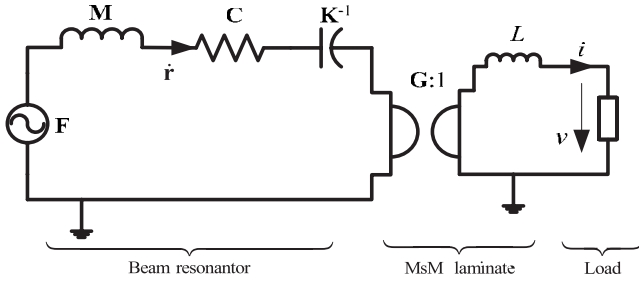


Figure 4. Equivalent circuit model of the MsM harvesting device.

where $m = (\rho_s t_s + \rho_M t_M)b$, t_s and t_M are the thickness of the substrate and the Metglas laminate, respectively.

Mechanical damping is added through a Rayleigh damping matrix \mathbf{C} . When multiple modes are considered, a proportional damping scheme is employed here to ensure uncoupling of the equations in the modal analysis [16, 17]:

$$\mathbf{C} = \alpha \mathbf{M} + \beta \mathbf{K} \quad (19)$$

where α and β are determined by

$$\zeta_i = \frac{\alpha}{2\omega_i} + \frac{\beta\omega_i}{2}, \quad i = 1, 2, \dots, N_r \quad (20)$$

where ζ_i is the damping ratio experimentally obtained from the frequency response of the beam structure [16].

Since the zero right-hand side of equation (16b) results from the short-circuit condition of the pick-up coil, an output voltage of v is added into equation (16b) for a practical case of the pick-up coil driving an electrical load. Inserting equations (18) and (19) back into equation (16a), the equations of motion for the harvesting device with electrical-mechanical coupling can be rearranged as

$$\mathbf{M}\ddot{\mathbf{r}} + \mathbf{C}\dot{\mathbf{r}} + \mathbf{K}\mathbf{r} + \mathbf{G}i = \mathbf{F} \quad (21a)$$

$$v = \mathbf{G}^T \dot{\mathbf{r}} - Li \quad (21b)$$

where \mathbf{M} , \mathbf{K} , and \mathbf{C} are $N_r \times N_r$ square matrices, \mathbf{G} , \mathbf{F} , and \mathbf{r} are $N_r \times 1$ column vectors, and v is the output voltage on an electrical load. In addition, \mathbf{G} can be considered as an equivalent gyrator converting mechanical velocity $\dot{\mathbf{r}}(t)$ into a voltage.

From equation (21), a generalized electromechanical circuit model is established for analyzing the MsM harvesting device as shown in figure 4, where mechanical modal matrices \mathbf{M} , \mathbf{C} and \mathbf{K}^{-1} are equivalent to electrical inductor, resistor and capacitor, respectively, while excitation force \mathbf{F} and generalized velocity $\dot{\mathbf{r}}$ are equivalent to the voltage and current, respectively.

According to figure 4 or equation (21), a vibration energy harvesting device, not limited to the MsM harvester, can be considered as a generalized four-terminal, two-port system as shown in figure 5. Generally speaking, the forcing vector \mathbf{F} and electrical voltage v are viewed as *efforts* which change magnitude between port terminals, while the velocity $\dot{\mathbf{r}}$ and electrical current i can be regarded as *flows*, which flow through the port [19]. The coupling term \mathbf{G}

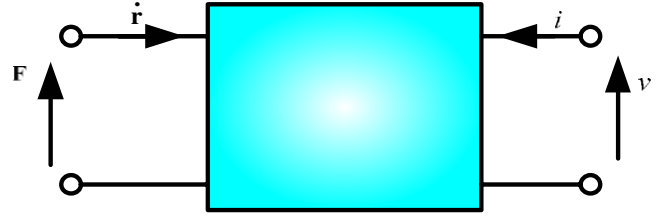


Figure 5. A generalized four-terminal, two-port system for a vibration energy harvester.

in equation (21a), converting the flow variables into effort variables (e.g. $\dot{\mathbf{r}}$ and i into v and \mathbf{F} , respectively), is analogous to an electromechanical gyrator, which converts variables across different states. In contrast, piezo-based harvesters convert variables within the same states (e.g. effort \mathbf{F} to effort v), so they are modeled as an electromechanical transformer in parallel connected with an equivalent capacitor [18, 20, 21].

For the cantilever beam, the displacement mode shape function ϕ_i is solved under the assumption of Euler-Bernoulli beam theory and the boundary conditions [17]:

$$\frac{d^4 \phi_i(x)}{dx^4} - \left(\frac{\lambda_i}{l}\right)^4 \phi_i(x) = 0 \quad (22)$$

where $(\lambda_i/l)^4 = m\omega_i^2/EI$ and EI is the equivalent weighted moment inertia of the substrate and Metglas laminate:

$$\text{at the clamped end : } \phi|_{x=0} = 0, \quad \phi'|_{x=0} = 0 \quad (23a)$$

$$\text{at the free end : } \phi''|_{x=l} = 0, \quad \phi'''|_{x=l} = 0. \quad (23b)$$

The general solution of equation (22) is given by

$$\phi_i = \eta_{i1} \cosh \lambda_i \frac{x}{l} + \eta_{i2} \sinh \lambda_i \frac{x}{l} + \eta_{i3} \cos \lambda_i \frac{x}{l} + \eta_{i4} \sin \lambda_i \frac{x}{l} \quad (24)$$

where the arbitrary constants, η_{ij} , $j = 1, \dots, 4$, are determined from the boundary conditions in equation (23):

$$\eta_{i1} = -\eta_{i3}, \quad \eta_{i2} = -\eta_{i4} \quad (25a)$$

$$\text{and } \begin{bmatrix} \cosh \lambda_i + \cos \lambda_i & \sinh \lambda_i + \sin \lambda_i \\ \sinh \lambda_i - \sin \lambda_i & \cosh \lambda_i + \cos \lambda_i \end{bmatrix} \begin{Bmatrix} \eta_{i1} \\ \eta_{i2} \end{Bmatrix} = 0. \quad (25b)$$

For nontrivial solution of η_{ij} , eliminating the determinant leads to

$$\cosh \lambda_i \cos \lambda_i + 1 = 0. \quad (26)$$

By numerically solving the above transcendental equation, successive values of λ_i correspond to the modes of the beam and the natural frequency of the i th mode can be calculated as

$$\omega_i = \lambda_i^2 \sqrt{EI/ml^4}. \quad (27)$$

The normal mode shape function of solution equation (24) can be rewritten as

$$\phi_i = \cosh \lambda_i \frac{x}{l} - \cos \lambda_i \frac{x}{l} - \eta_i \left(\sinh \lambda_i \frac{x}{l} - \sin \lambda_i \frac{x}{l} \right) \quad (28)$$

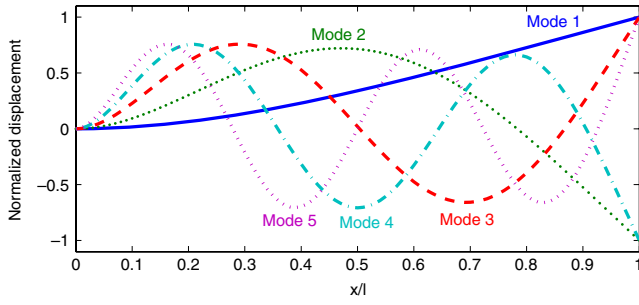


Figure 6. First five mode shapes of a cantilever beam.

Table 2. Mode shape constants of λ_i and η_i for a cantilever beam.

| Mode no. i | λ_i | η_i |
|--------------|-----------------|---------------|
| 1 | 1.875 104 07 | 0.734 095 514 |
| 2 | 4.694 091 13 | 1.018 467 319 |
| 3 | 7.854 757 44 | 0.999 224 497 |
| 4 | 10.995 540 73 | 1.000 033 553 |
| 5 | 14.137 168 39 | 0.999 998 550 |
| >5 | $(2i - 1)\pi/2$ | ≈ 1.0 |

where $\eta_i = \eta_{i2}/\eta_{i1} = (\cosh \lambda_i + \cos \lambda_i)/(\sinh \lambda_i + \sin \lambda_i)$. Table 2 lists the mode shape constants of λ_i and η_i for a cantilever beam from the handbook [22]. Figure 6 displays the first five mode shapes of a cantilever beam.

By taking the mode shape function of equation (28) and using integral formulae containing ϕ_i from the handbook [22], the closed-form of modal matrices can be further simplified as

$$\mathbf{M} = [M_{ij}] = \left[\int_{V_s} \rho_s \phi_i \phi_j, dV_s + \int_{V_M} \rho_M \phi_i \phi_j dV_M \right] = \langle M_s + M_M \rangle = \langle M \rangle \quad (29a)$$

$$\mathbf{K} = [K_{ij}] = \left[\int_{V_s} E_s \phi_i'' \phi_j'' z^2 r dV_s + \int_{V_M} E^H \phi_i'' \phi_j'' z^2 dV_M \right] = \frac{EI}{l^3} \langle \lambda_i^4 \rangle \quad (29b)$$

$$\mathbf{C} = \alpha \langle M \rangle + \frac{\beta EI}{l^3} \langle \lambda_i^4 \rangle \quad (29c)$$

$$\mathbf{G} = \{G_i\} = \frac{zNd^* E^H A_M}{l} \left\{ \int_0^l \phi_i'^T(x) dx \right\} = \frac{2Nd^* E^H A_M h_M}{l^2} \{(-1)^{i+1} \eta_i \lambda_i\}^T \quad (29d)$$

$$\mathbf{F} = \{F_i\} = \left\{ -\ddot{w}_B m \int_0^l \phi_i^T(x) dx \right\} = -2M \ddot{w}_B \{\eta_i / \lambda_i\}^T \quad (29e)$$

where $[]$ and $\langle \rangle$ indicate square and diagonal matrices, respectively, $\{ \}$ denotes row vector and M is the total mass of the copper substrate and Metglas laminate.

The following conclusions can be drawn from equation (29).

- (1) Except for \mathbf{M} , all the other closed forms of modal parameters including \mathbf{K} , \mathbf{C} , \mathbf{G} and \mathbf{F} of the MsM harvesting are functions of mode shape constants λ_i and η_i associated with the i th individual normal mode.

- (2) Because the mechanical displacement is decomposed into N_r generalized coordinates $\mathbf{r}(t)$, the normal mode transformation enables us to change the set of coupled N_r -DOF equations of motion into a set of N_r uncoupled 1-DOF equations of motion.
- (3) The governing equation (21) is valid not only below the fundamental natural frequency, but also in a wide frequency range up to any high natural frequency ω_{N_r} . The natural frequency matrix from equation (29) can be calculated as $[\omega_i] = \sqrt{\mathbf{K}\mathbf{M}^{-1}} = \langle \lambda_i^2 \sqrt{EI/MI^3} \rangle$, which is identical to equation (27).

Equation (22) can be expressed in frequency domain as

$$-\omega^2 \mathbf{M} \tilde{\mathbf{r}} + j\omega \mathbf{C} \tilde{\mathbf{r}} + \mathbf{K} \tilde{\mathbf{r}} + \mathbf{G} \tilde{\mathbf{i}} = \tilde{\mathbf{F}} \quad (30a)$$

$$\tilde{v} = j\omega \mathbf{G}^T \tilde{\mathbf{r}} - j\omega L \tilde{i} \quad (30b)$$

where \sim indicates the Fourier transform of the parameter.

Following the procedure in section 3.1, the total internal energy of the MsM harvesting device is given by

$$\mathcal{E} = \tilde{\mathbf{r}}^T \tilde{\mathbf{F}} + \frac{1}{j\omega} \tilde{v} \tilde{i}. \quad (31)$$

Substitution of $\tilde{\mathbf{F}}$ and \tilde{v} by equation (30) yields

$$\mathcal{E} = \tilde{\mathbf{r}}^T (\mathbf{K} - \omega^2 \mathbf{M} + j\omega \mathbf{C}) \tilde{\mathbf{r}} + \tilde{\mathbf{r}}^T \mathbf{G} \tilde{i} + \mathbf{G}^T \tilde{\mathbf{r}} - L \tilde{i}^2 = \mathcal{E}_m + \mathcal{E}_{me} + \mathcal{E}_{em} + \mathcal{E}_e \quad (32)$$

where subscripts m, e and me (or em) indicate the mechanical, electrical and mutual electromechanical energy, respectively. Note that the negative sign in equation (32) indicates 180° phase delay of electrical energy contained by the equivalent inductance of the coil.

Then a global electromechanical coupling coefficient k_g of the harvesting device can be introduced as

$$k_g^2 = \frac{\mathcal{E}_{me} \mathcal{E}_{em}}{\mathcal{E}_m \mathcal{E}_e} = \frac{\tilde{\mathbf{r}}^T \mathbf{G} \mathbf{G}^T \tilde{\mathbf{r}}}{L \tilde{\mathbf{r}}^T (\mathbf{K} - \omega^2 \mathbf{M} + j\omega \mathbf{C}) \tilde{\mathbf{r}}}. \quad (33)$$

Because the MsM harvesting device is operated at its individual natural frequency ω_i , equation (21) can be reduced to a 1-DOF system associated with the i th normal mode:

$$M_i \ddot{r}_i + C_i \dot{r}_i + K_i r_i + G_i \dot{i}_i = F_i \quad (34a)$$

$$v_i = G_i \dot{r}_i - L \dot{i}_i. \quad (34b)$$

To further simplify equation (33) for a given mode, equation (34) can be grouped in the Laplace domain as

$$\begin{Bmatrix} \bar{F}_i \\ \bar{V}_i \end{Bmatrix} = \begin{bmatrix} Z_m & G_i \\ G_i & -sL \end{bmatrix} \begin{Bmatrix} \bar{U}_i \\ \bar{I}_i \end{Bmatrix} \quad (35)$$

where the overbar indicates the variable in Laplace domain, s is the Laplace variable, $Z_m = M_i s + C_i + K_i/s$ is the mechanical impedance, \bar{V}_i and \bar{I}_i are the unknown output voltage and current, \bar{U}_i is the unknown relative velocity of \dot{r}_i in the Laplace domain and $\bar{F} = 2s^2 M w_B \eta_i / \lambda_i$ is the base excitation force with the known base displacement w_B . Therefore equation (35) has two equations for three unknowns: \bar{V}_i , \bar{I}_i and \bar{U}_i . To obtain the unique solution, another relation needs to be introduced.

The global electromechanical coupling coefficient k_g for the i th vibration mode is derived from equation (33):

$$k_g = \frac{\mathcal{E}_{mM}}{\sqrt{\mathcal{E}_m \mathcal{E}_M}} = \frac{G}{\sqrt{s L Z_m}}. \quad (36)$$

At resonance frequency ω_i , it can be further reduced via equations (17d) and (29d):

$$k_g^2 = \frac{4\sqrt{M}E^H A_M h_M^2}{C_i \sqrt{EI} l^3} \eta_i^2 k^2. \quad (37)$$

From equation (37), several useful guidelines for designing MsM harvesting devices can be concluded:

- (1) The energy conversion efficiency for the MsM harvester is proportional to k_g^2 . Meanwhile, the global electromechanical coupling coefficient k_g is linearly proportional to the material coupling coefficient k .
- (2) Although k_g is not an explicit function of frequency ω_i , it is proportional to the value of the mode shape constant η_i . According to table 2, this result implies that, for the same device, the fundamental vibration mode offers the lowest k_g . On the other hand, the influence of η_i on k_g is not significant because of $\eta_i \approx 1.0$, $i \geq 2$.
- (3) k_g is independent of the number of turns of the pick-up coil, N . However, N should not be too small in the actual design; otherwise the induced voltage in the coil will be too small to be rectified by the electronic circuit. Furthermore, a large number of N can guarantee the accuracy of equation (15) due to the assumption of long solenoid coil.
- (4) The thicker the Metglas layer is, the higher the k_g that results.

3.3. Model extension for a cantilever beam with a tip mass

Because ambient vibrations are usually at low frequencies, it is necessary to add a tip mass at the free end of the MsM harvesting device to reduce its fundamental frequency. Another advantage of using the tip mass is to increase the forcing vector \mathbf{F} , leading to larger harvested energy. The model derived in section 3.2 needs to be further extended or modified. The analysis with the additional tip mass is covered briefly based on the previous work [18, 23, 24].

As illustrated in figure 7, the mass center of a tip mass M_0 with the small length of l_0 does not coincide with that of the free end of the beam, O. The Euler–Bernoulli beam theory and the normal mode superposition can still be employed to determine the transverse displacement $w(x, t)$: thus equation (24) governing the beam $0 \leq x \leq l$ is still valid and not repeated here. However, the arbitrary constants η_{ij} , $j = 1, \dots, 4$ are solved from the modified boundary conditions with the rigid tip mass. Assume that both the beam and the tip mass are uniform in the axial direction with mass per length of m and m_0 , respectively. The boundary conditions at the clamped end are the same as equation (23a), so equation (25a) is valid for this case. In addition, the boundary conditions at the point where the beam end and the

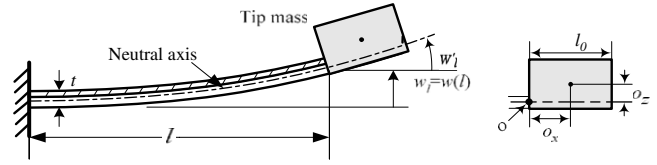


Figure 7. Uniform cantilever beam with a tip mass.

tip mass are connected are obtained by a variational method as

$$EI w_l'' = \omega^2 I_0 w_l' + \omega^2 S_0 w_l \quad (38a)$$

$$EI w_l''' = -\omega^2 M_0 w_l - \omega^2 S_0 w_l' \quad (38b)$$

where $M_0 = m_0 l_0$, $S_0 = M_0 o_x$, $I_0 = J + M_0(o_x^2 + o_z^2)$ and $J = M_0(l_0^2 + t_0^2)/12$ is the mass moment of inertia of the tip mass around its mass center, and t_0 and l_0 are the thickness and length of the tip mass, respectively. By introducing the nondimensional ratios $\hat{M}_0 = M_0/ml$, $\hat{S}_0 = S_0/ml^2$ and $\hat{I}_0 = I_0/ml^3$, the boundary conditions of equation (38) yield the following matrix equation:

$$\begin{bmatrix} a_{11} & a_{12} \\ a_{21} & a_{22} \end{bmatrix} \begin{Bmatrix} \eta_{i3} \\ \eta_{i4} \end{Bmatrix} = 0 \quad (39)$$

where

$$a_{11} = (\cosh \lambda_i + \cos \lambda_i) + \lambda_i^3 \hat{I}_0 (-\sinh \lambda_i - \sin \lambda_i) + \lambda_i^2 \hat{S}_0 (-\cosh \lambda_i + \cos \lambda_i) \quad (40a)$$

$$a_{12} = (\sinh \lambda_i + \sin \lambda_i) + \lambda_i^3 \hat{I}_0 (-\cosh \lambda_i + \cos \lambda_i) + \lambda_i^2 \hat{S}_0 (-\sinh \lambda_i + \sin \lambda_i) \quad (40b)$$

$$a_{21} = (\sinh \lambda_i - \sin \lambda_i) + \lambda_i \hat{M}_0 (\cosh \lambda_i - \cos \lambda_i) + \lambda_i^2 \hat{S}_0 (\sinh \lambda_i + \sin \lambda_i) \quad (40c)$$

$$a_{22} = (\cosh \lambda_i + \cos \lambda_i) + \lambda_i \hat{M}_0 (\sinh \lambda_i - \sin \lambda_i) + \lambda_i^2 \hat{S}_0 (\cosh \lambda_i - \cos \lambda_i) \quad (40d)$$

λ_i can be numerically solved by eliminating the determinant of the matrix in equation (39). Then substitution of a new λ_i and $\eta_i = a_{11}/a_{12}$ into equations (27) and (28) yields natural frequencies and normal mode shapes, respectively. If there is no tip mass attached at the free end, i.e. \hat{M}_0 , \hat{S}_0 and \hat{I}_0 are all zero, equation (39) is reduced to equation (25b).

A numerical example illustrates the effects of tip-mass-to-beam-mass ratio \hat{M}_0 on the mode shapes and structural natural frequencies as shown in figures 8 and 9, respectively. The parameters in the simulation are chosen as $o_x = 0.1l$, $o_z = 0.066l$, $l_0 = 2o_x$, $t_0 = 2o_x$ and \hat{M}_0 varies in a range of $[0, 10]$. From figure 8, especially the last three plots, it can be seen that the larger \hat{M}_0 leads to a longer effective wavelength of the mode shapes; on the other hand, the amplitude at the connection point of tip mass and beam end approaches zero when mass ratio \hat{M}_0 increases, because infinite \hat{M}_0 leads to a clamp end boundary condition. The dependence of natural frequencies on the ratio of tip mass to beam mass is shown in figure 9, where the frequency of each mode is normalized by the natural frequencies of the cantilever beam without tip mass, i.e. at the condition of $\hat{M}_0 = 0$. It can be seen that (1) mass

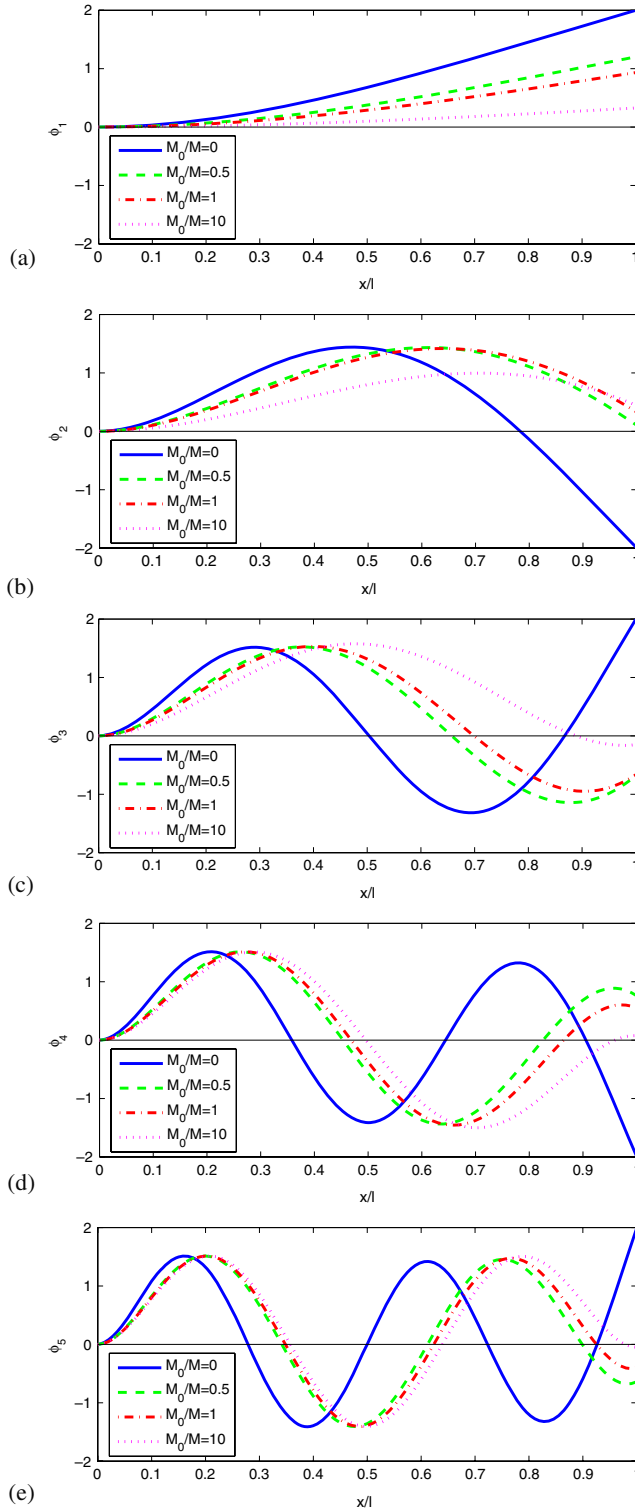


Figure 8. First five mode shapes of a cantilever beam with different tip-to-beam mass ratios.

ratio \hat{M}_0 remarkably reduces the structural natural frequencies and it steeply decays in the range of $\hat{M}_0 < 0.5$ and (2) in the range of \hat{M}_0 beyond 0.5, the lower modes, the larger influence and a flat region can be observed in the fourth and fifth modes.

The effective mass of the beam can be obtained from a similar variational approach discussed in section 3.2. The

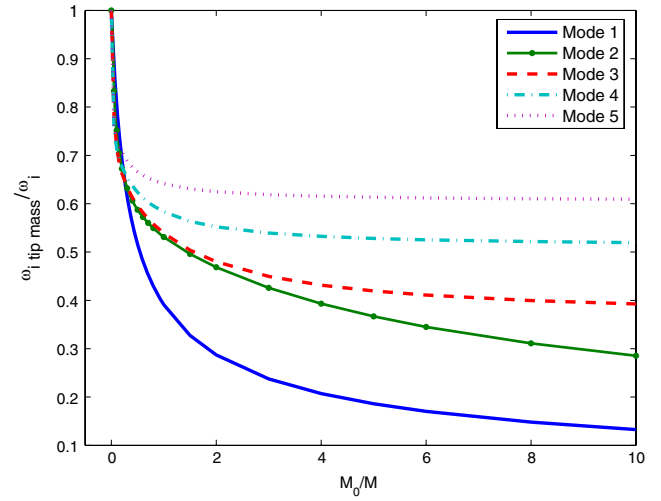


Figure 9. Effect of tip-to-beam mass ratio, M_0/M , on the structural natural frequencies.

modal mass matrix equation (17a) should be replaced by the following equation when a tip mass is attached to the cantilever beam:

$$\mathbf{M} = \int_{V_s} \rho_s \boldsymbol{\phi}^T(x) \boldsymbol{\phi}(x) dV_s + \int_{V_M} \rho_M \boldsymbol{\phi}^T(x) \boldsymbol{\phi}(x) dV_M + M_0 \boldsymbol{\phi}^T(l) \boldsymbol{\phi}(l) + 2S_0 \boldsymbol{\phi}^T(l) \boldsymbol{\phi}'(l) + I_0 \boldsymbol{\phi}^T(l) \boldsymbol{\phi}''(l). \quad (41)$$

The effective stiffness matrix \mathbf{K} has the same expression as equation (17b) except for the mode shape function.

Finally, the external work term should be re-evaluated to include the inertial loading due to the tip mass. Equation (18) needs to be updated by taking into account the contribution of both the uniform cantilever beam and the tip mass. The displacement of the tip mass is calculated in terms of the displacement and rotation of the tip of the beam:

$$\mathbf{F} = -\ddot{\mathbf{w}}_B \left[m \int_0^l \boldsymbol{\phi}^T(x) dx + m_0 \int_l^{l+l_0} \boldsymbol{\phi}^T(l) dx + m_0 \int_l^{l+l_0} x \boldsymbol{\phi}^T(l) dx \right]. \quad (42)$$

According to figure 9, equations (41) and (42), it has been theoretically proved that the tip mass produces two major effects. First, it significantly reduces the natural frequencies of the beam; in other words it is feasible to change the natural frequencies by adjusting the tip mass. Second, the tip mass induces an additional excitation force under the same base excitation.

3.4. Power analysis

Because equation (35) has two equations for three unknowns, another relation associated with the characteristic of an electrical load is required to obtain a unique solution. A pure resistive load is unable to contain the converted energy but dissipates it into Joule heat. In general, the analysis is conveniently performed at the steady state for a resistive load in the Laplace, or frequency, domain. On the other hand, an ultracapacitor, or capacitive load, can collect the

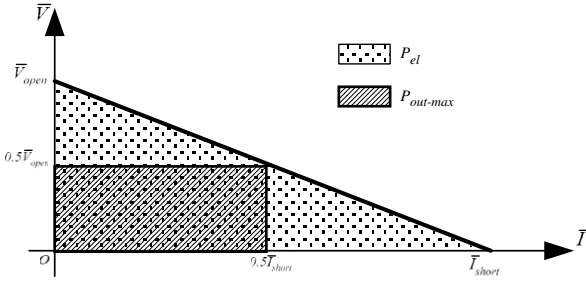


Figure 10. The volt-amp characteristic of the harvesting device.

converted energy. A charging storage device is in a transient state, so it should be modeled by original ODEs (ordinary differential equations) in the time domain. Although the following formulation is established for the harvesting device vibrating around its individual natural frequency ω_i , it can be extended for general non-resonance frequency by using the corresponding parameters in equation (29).

3.4.1. Resistive load. Eliminating velocity \dot{U}_i in equation (35) gives the volt-amp characteristic of the harvesting device as shown in figure 10:

$$\bar{V}_i = -(sL + G_i^2/Z_m)\bar{I}_i + G_i\bar{F}_i/Z_m. \quad (43)$$

The open-circuit voltage and short-circuit current can be obtained from equation (43) by setting $\bar{I}_i = 0$ and $\bar{V}_i = 0$, respectively:

$$\bar{V}_{\text{open}} = G_i\bar{F}_i/Z_m \quad (44a)$$

$$\bar{I}_{\text{short}} = G_i\bar{F}_i/(sLZ_m + G_i^2). \quad (44b)$$

In figure 10, the dotted area under the volt-amp characteristic line is associated with converted electrical power:

$$P_{\text{el}} = \frac{1}{2}\bar{V}_{\text{open}}\bar{I}_{\text{short}} = \frac{G_i^2\bar{F}_i^2}{2Z_m(sLZ_m + G_i^2)}. \quad (45)$$

For a resistive load R , all the above equations are valid in steady state. The maximum output power from the harvesting device can be easily obtained by maximizing the rectangular in the slashed region in figure 10:

$$P_{\text{out-max}} = \frac{\bar{V}_{\text{open}}\bar{I}_{\text{short}}}{4} = \frac{G_i^2\bar{F}_i^2}{4Z_m(sLZ_m + G_i^2)} \quad (46)$$

and the corresponding optimized load is the slope of the line connecting the origin and $(0.5\bar{I}_{\text{short}}, 0.5\bar{V}_{\text{open}})$ in figure 10:

$$R_{\text{op}} = \frac{\bar{V}_{\text{open}}}{\bar{I}_{\text{short}}} = (sLZ_m + G_i^2)/Z_m. \quad (47)$$

To compute the general frequency response, equation (30) can be expressed in the frequency domain as

$$-\omega^2\mathbf{M}\tilde{\mathbf{r}} + j\omega\mathbf{C}\tilde{\mathbf{r}} + \mathbf{K}\tilde{\mathbf{r}} + \mathbf{G}\tilde{\mathbf{i}} = \tilde{\mathbf{F}} \quad (48a)$$

$$R\tilde{\mathbf{i}} = j\omega\mathbf{G}^T\tilde{\mathbf{r}} - j\omega L\tilde{\mathbf{i}}. \quad (48b)$$

Solving the above equations, the frequency response of the transverse displacement can be obtained:

$$\tilde{w}(x, \omega) = \boldsymbol{\phi}(x)\tilde{\mathbf{r}}(\omega) \quad (49)$$

where $\tilde{\mathbf{r}}$ is solved from equation (30):

$$\tilde{\mathbf{r}} = \left[\mathbf{K} - \omega^2\mathbf{M} + j\omega\mathbf{C} + \frac{j\omega}{R + j\omega L}\mathbf{G}\mathbf{G}^T \right]^{-1} \tilde{\mathbf{F}}. \quad (50)$$

3.4.2. Ultracapacitor. Equation (46) is not desirable in actual energy harvesting because all scavenged electrical power is dissipated in the resistor R . Examining a capacitive load C_s , the energy storage device, is of importance for assessing the MsM's charging capability. Due to the transient state of charging the energy storage C_s , the original ODEs in time domain are employed in modeling

$$\begin{aligned} F_i &= M_i\ddot{r}_i + C_i\dot{r}_i + K_i r_i + G_i i_i \\ v_i &= G_i\dot{r}_i - L_i\dot{i}_i \\ i_i &= C_s\dot{v}_i \end{aligned} \quad (51)$$

where $F_i = 2M\eta_i\omega_i^2 w_B \sin \omega_i t / \lambda_i$ is the equivalent input force from the base. Then equation (51) can be rearranged as a set of first-order ODEs in terms of the matrix form in state space:

$$\begin{Bmatrix} \dot{r}_i \\ \ddot{r}_i \\ \dot{v}_i \\ \ddot{v}_i \end{Bmatrix} = \begin{bmatrix} 0 & 1 & 0 & 0 \\ \frac{-K_i}{M_i} & \frac{-C_i}{M_i} & 0 & \frac{-G_i C_s}{M_i} \\ 0 & 0 & 0 & 1 \\ 0 & \frac{-G_i}{L C_s} & \frac{1}{L C_s} & 0 \end{bmatrix} \begin{Bmatrix} r_i \\ \dot{r}_i \\ v_i \\ \dot{v}_i \end{Bmatrix} + \begin{Bmatrix} 0 \\ \frac{2\eta_i\omega_i^2 w_B}{\lambda_i} \sin \omega_i t \\ 0 \\ 0 \end{Bmatrix} \quad (52)$$

with initial conditions

$$r(0) = \dot{r}(0) = 0 \quad \text{and} \quad v(0) = \dot{v}(0) = 0. \quad (53)$$

Generally the closed-form solution of v from equation (53) is unlikely to obtain, but a numerical solution can be simply computed by finite difference algorithms such as the Runge-Kutta method. The ideal rectification without the forward voltage drop of diodes can be considered by substituting $\sin \omega_i t$ with its absolute values in equation (53).

4. Circuit design

As shown in figure 11, the electric circuit for the MsM harvester consists of three components: a set of voltage quadruplers as the recharging circuit, a 3 F ultracapacitor for energy storage and a smart voltage regulator. The major advantages of ultracapacitors over chemical rechargeable batteries include instant charging, about 10 times higher charge/discharge efficiency, semi-permanent life cycles, lower cost and smaller size (1/7 of AA batteries) [12]. Because the ultracapacitor holds the accumulated opposite charges apart to store energy, still in terms of electric potential energy, chemical reactions are not needed.

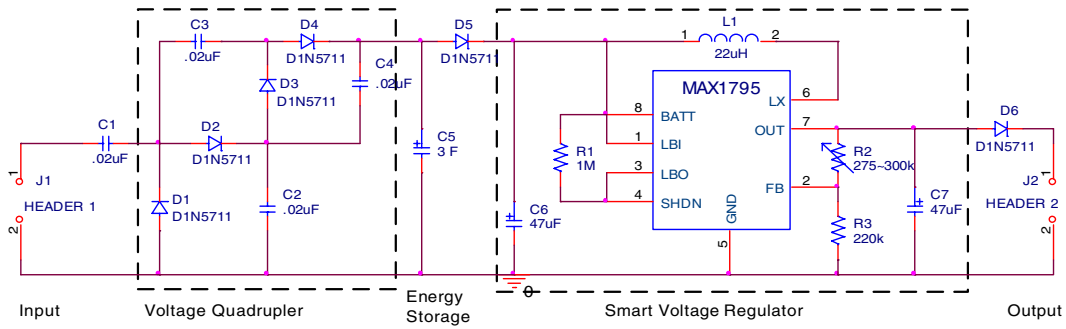


Figure 11. Energy harvesting circuit.

The AC voltage from the MsM pick-up coil is less than 1 V, which is insufficient to charge the ultracapacitor C_5 . Although half-wave or full-wave rectifier bridges can convert AC to DC voltage, the DC voltage becomes even lower because of forward voltage drops on the diodes. To overcome the obstacle, a simple voltage quadrupler circuit is introduced in figure 11. When the AC voltage from J_1 is in negative polarity, diodes D_1 and D_3 are in the on state, while D_2 and D_4 are in the off state; then capacitors C_1 and C_3 are charged up to virtually the peak supply voltage V_m . When the polarity changes to positive, C_1 and C_3 are unable to discharge via D_1 and D_3 , respectively; D_2 is on so the voltage on C_1 is added to that of the AC voltage, charging C_2 to twice the peak value. Likewise, C_4 is charged to $2V_m$ as well. Because C_2 and C_4 are unable to discharge, it tends to hold the DC voltage $4V_m$ cross the ultracapacitor C_5 . In practice, due to the inevitable forward voltage drop on each diode, the DC voltage level on C_5 is never quite charged to $4V_m$, but will come very close. During the following positive half-period, any discharge of C_2 and C_4 to a load is replenished via C_1 and C_3 ; in this respect C_2 and C_4 behave like smoothing capacitors, which acts like a rectifier filter reducing ripples in the output voltage. Therefore a voltage quadrupler can achieve AC–DC rectification, filtering and increasing the DC voltage level simultaneously [25].

The smart regulator is an important logic unit in the harvester module to clamp the output DC voltage level of C_5 , optimize charging performance, and self-turn on and off. The key IC on the PCB is MAX1795, a high efficiency step-up DC–DC converter. It features self-shutdown circuitry, which fully disconnects the output from the input, improves efficiency and eliminates costly peripheral components. MAX1795 only consumes 25 μ A quiescent current and 2 μ A shutdown current. The IC's conversion efficiency was reported to reach 95%. For additional in-system flexibility, a voltage monitoring comparator (LBI/LBO pins) remains active even when the DC–DC converter is in shutdown [26]. By setting the peripheral circuit as shown in figure 11, the output voltage level from MAX1795 can be adjustable and the variable resistor R_1 is determined by

$$R_1 = R_2 (V_{out}/V_{FB} - 1) \quad (54)$$

where $V_{FB} = +1.245$ V, V_{out} may range from +2 to +5.5 V, and R_2 should be chosen less than 250 k Ω . On the other hand, V_{out} can be fixed to 3.3 V or 5.0 V by directly connecting the

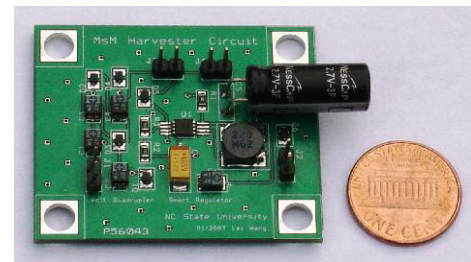


Figure 12. Actual PCB of the MsM harvesting circuit.

FB pin to OUT or GND, respectively. Connecting pin BATT to LBI, the lowest self-startup can be guaranteed from +0.85 V. In other words, MAX1795 is operating when the voltage level on pin BATT is higher than +0.85 V. By connecting pin LBO to SHDN, the MAX1795 can self-shutdown when the input voltage drops below a preset threshold +0.85 V. Schottky diodes D_5 and D_6 prevent the reverse current. C_6 and C_7 are input and output filter capacitors, respectively. L_1 is the external inductor for MAX1795 [26]. As shown in figure 12, the actual PCB has a compact size, 25 mm \times 35 mm.

5. Experimental studies

The experimental set-up and a close-up of the actual harvesting device are shown in figures 13(a) and (b), respectively. An Agilent 33220A function generator excites a sinusoidal signal. Then the signal is sent to a TDS420A oscilloscope and a K-H7602 amplifier to drive the LDS V201 vibration shaker. The MsM harvesting device with a 100-turned pick-up coil is screwed on the top of the LDS V201 shaker. Meanwhile a Micro-Epsilon optoNCDT 1607 laser sensor measures the time-varying displacement of the MsM harvester. The voltage signals of the laser sensor are recorded by the digital oscilloscope.

5.1. Powering a resistive load

In the resistive load test, six layers of Metglas 2605SC (total thickness 0.3 mm including adhesive) without the copper substrate are laminated with 3M[®] DP-810 adhesive and a seismic mass is attached at the free end of the cantilever beam such that the fundamental resonance frequency is as low as

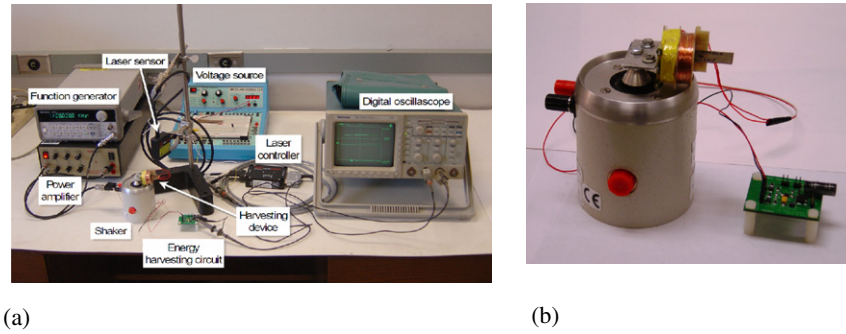


Figure 13. (a) Experimental set-up and (b) a close-up of the actual harvesting device.

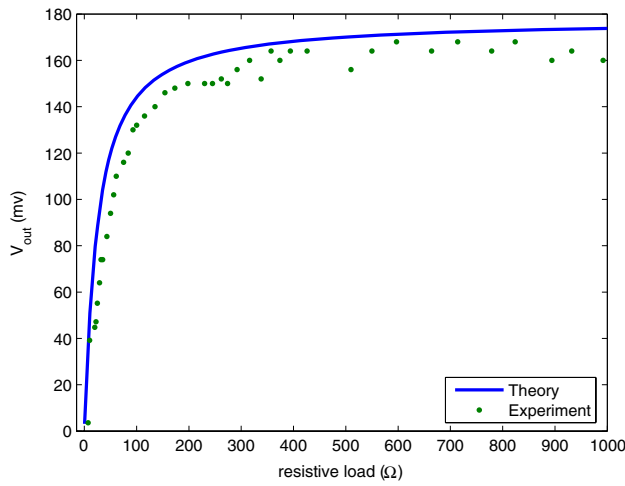


Figure 14. Comparison of theoretical and experimental results on output voltage under 58.1 Hz and 1g acceleration.

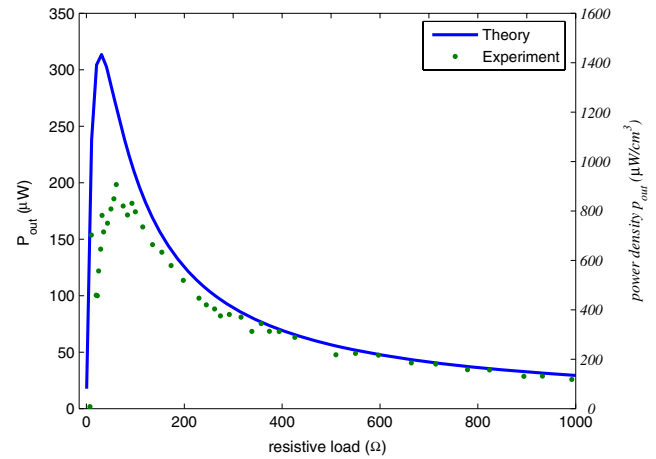


Figure 15. Comparison of theoretical and experimental results on output power under 58.1 Hz and 1g acceleration.

58 Hz. In this test, rectification and harvesting circuits are excluded. The output voltage and power on external resistive loads are shown in figures 14 and 15, respectively, where the solid line represents the theoretical prediction and dots indicate experimental results. From figure 15, it can be seen that the maximum output voltage is about 0.15 V, the maximum output power reaches $200 \mu\text{W}$ and the corresponding power density is $900 \mu\text{W cm}^{-3}$ (with respect to the active material volume), which is higher than that of most piezo-based harvesters [4]. The voltage is, however, lower than the forward voltage drop of diodes; thus it is not practical in actual applications. Increasing the resonance frequency and using a voltage multiplier can be a viable solution. The discrepancy of maximum power between theory prediction and experimental measurement may result from the measured equivalent damper coefficient. The optimal resistive load R_{op} can be calculated from equation (47), and it is normally a very small value (less than 100Ω) compared to that of a piezo-based harvester ($>1 \text{ M}\Omega$). Thus, unlike a piezo-based harvester, the MsM harvester of this design is not well suited to drive a high resistive load.

5.2. Charging the ultracapacitor

The aim of conducting the second test is to assess the charging ability of the MsM harvester on the ultracapacitor at a relatively

high frequency ($\sim 1 \text{ kHz}$). An eight-layered Metglas 2605SC laminate (total active material volume of 0.95 cm^3) without the seismic mass is bonded on a copper substrate (0.4 mm thickness). The output from the pick-up coil is connected to the energy harvesting circuit for storage and regulation.

Figure 16 shows the experimental waveforms of the tip displacement of the harvester, AC voltage from the pick-up coil and DC output from the voltage quadrupler circuit. A little nonlinear behavior in the measured tip displacement, as shown in the top plot, may result from the phase distortion of the K-H7602 power amplifier. Under vibration with a resonance frequency of 1.1 kHz and peak acceleration of 8.06 m s^{-2} (or, 0.82 g), the amplitude of the tip displacement, measured by the Micro-Epsilon optoNCDT 1607 laser sensor, is about 0.05 mm as shown in the top plot, and the induced AC voltage from the pick-up coil has an amplitude of 0.7 V , represented by a dashed line. Theoretically, the DC output from the voltage quadrupler should be 2.8 V . However, due to the forward voltage drop of each BAT54WS diode, the actual DC voltage level can reach 2.3 V .

The last experiment is to evaluate the MsM harvester's charging capability of the ultracapacitor and test the performance of the smart voltage regulator. After the voltage on ultracapacitor C_5 reaches 2.3 V , a $1 \text{ k}\Omega$ resistive load is connected to the smart regulator for measuring the discharge

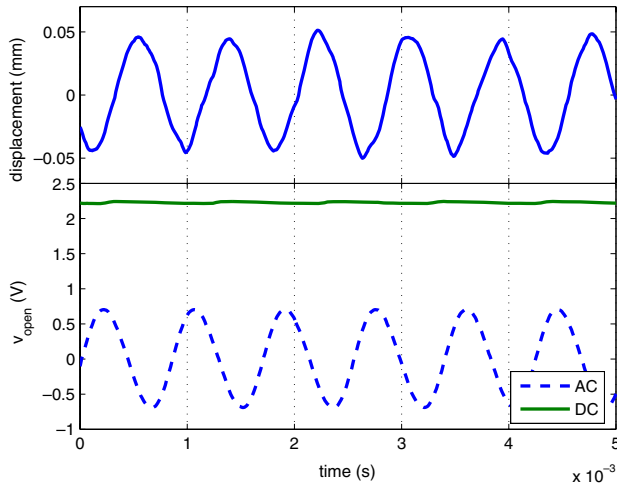


Figure 16. Tip displacement of the MsM harvester, AC voltage from the pick-up coil and DC output from the voltage quadrupler.

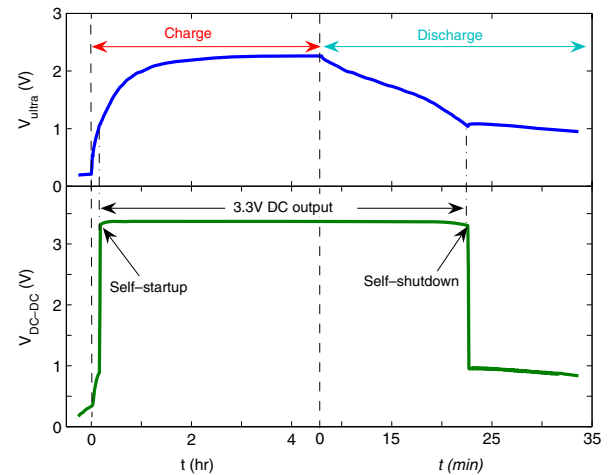


Figure 17. Experimental results of the charging/discharging of the ultracapacitor and output performance of the smart voltage regulator.

history of C_5 and the output voltage level. Figure 17 shows the experimental voltage history on C_5 in the upper plot and the recorded DC voltage output from the voltage regulator in the lower plot. From the upper plot of figure 17, it is evident that the voltage on C_5 contains an exponentially charging cycle and a discharging cycle with an almost linear decay rate. When the voltage on C_5 is higher than 0.9 V, the smart regulator can self-startup and the output voltage is clamped at 3.3 V as shown in the lower plot. On the other hand, if the voltage on C_5 is less than the threshold value of 0.9 V, the smart regulator will shutdown by itself to reduce dissipated energy. The voltage on the ultracapacitor may fluctuate, but the output voltage level from the smart voltage regulator is fixed at a certain constant value until the voltage on the ultracapacitor is less than 0.9 V. Because the harvested power from the vibration is small, it takes about 3.5 h to fully charge the 3 F ultracapacitor. Correspondingly, the average power and the average power density for charging the capacitive energy storage can achieve $576 \mu\text{W}$ and $606 \mu\text{W cm}^{-3}$ (with respect to the active material volume), respectively, which are higher than those of most piezo-based harvesters [4], typically about two times higher than [1]. Note that the volume of the Metglas laminate is used in calculating the power density.

6. Conclusions

The new MsM vibration harvester holds promise as an alternative scheme of energy harvesting apart from the common piezoelectric harvesting approaches. The MsM energy harvester contains a transversely annealed Metglas 2605SC laminated beam and an electronic circuit on a PCB for interfacing with a wireless sensor. Meanwhile, a generic architecture for energy-harvesting-based sensors is proposed. A closed form of governing equations of motion for the MsM harvesting device to analyze the MsM harvesting device is derived by Hamilton's principle in conjunction with the normal mode superposition method based on the Euler–Bernoulli beam theory. To enhance the magnetomechanical coupling, a

Metglas 2605SC is transversely annealed by a strong magnetic field in the width direction of the ribbon. The annealed ribbon does not require a bias magnetic field, thereby reducing the harvester size. According to the experimental results, the average power and power density during charging the ultracapacitor can achieve $576 \mu\text{W}$ and $606 \mu\text{W cm}^{-3}$ (with respect to the active material volume) at high frequency, which compete favorably with piezoelectric vibration harvesters. However, several challenges of the current design still need to be overcome. First, due to rapid quenching, the thickness of the standard Metglas ribbons used in this study is limited to $18 \mu\text{m}$. The adhesive undermines the magnetomechanical coupling and induces residual stress. Thicker Metglas can decrease the number of laminated layers, reducing the load transfer loss of the adhesive and further enhancing the output performance. Second, the dimension of the pick-up coils needs to be reduced. The recently developed printed tape coils by the MEMS technique could be a possible solution [27]. In addition, a future study should also include measuring the actual energy conversion ratio, comparing with the theoretical prediction and incorporating the power switching and power management components in WISP (wireless intelligent sensor platform) [28], which has been developed at NCSU for a self-contained wireless sensor.

Acknowledgments

This research is supported by the National Science Foundation under grant nos. CMS-0329878 and CMMI-0654233 (Program Manager: Dr S C Liu). The authors would like to thank Dr R Hasegawa of Metglas®, Inc. for generously providing Metglas ribbons and valuable technical support. Special thanks go to Advanced Circuits, Inc. for sponsoring the PCB.

References

- [1] Roundy S, Wright P K and Rabaey J M 2004 *Energy Scavenging for Wireless Sensor Networks: With Special Focus on Vibrations* (Boston: Kluwer–Academic)

- [2] Glynne-Jones P and White N M 2001 Self-powered systems: a review of energy sources *Sensor Rev.* **21** 91–7
- [3] Sodano H A, Inman D J and Park G 2004 A review of power harvesting from vibration using piezoelectric materials *Shock Vib. Dig.* **36** 197–205
- [4] Beeby S P, Tudor M J and White N M 2006 Energy harvesting vibration sources for microsystems applications *Meas. Sci. Technol.* **17** R175–95
- [5] Du Trâmolet de Lacheisserie E 1993 *Magnetostriction: Theory and Applications of Magnetoelasticity* (Boca Raton, FL: CRC Press)
- [6] Metglas, Inc 2007 Magnetic alloy 2605SC (Iron-based) <http://www.metglas.com/>
- [7] Staley M E and Flatau A B 2005 Characterization of energy harvesting potential of Terfenol-D and Galfenol *Proc. SPIE* **5764** 630–40
- [8] Huang J, O’Handley R C and Bono D 2003 New, high-sensitivity, hybrid magnetostrictive/electroactive magnetic field sensors *Proc. SPIE* **5050** 229–37
- [9] Bayrashev A, Robbins W P and Ziaie B 2004 Low frequency wireless powering of microsystems using piezoelectric–magnetostrictive laminate composites *Sensors Actuators A* **114** 244–9
- [10] Modzelewski C, Savage H T, Kabacoff L T and Clark A E 1981 Magnetomechanical coupling and permeability in transversely annealed Metglas 2605 alloys *IEEE Trans. Magn.* **17** 2837–9
- [11] Meeks S W and Hill J C 1983 Piezomagnetic and elastic properties of metallic-glass alloys $\text{Fe}_{67}\text{Co}_{18}\text{B}_{14}\text{Si}_1$ and $\text{Fe}_{81}\text{B}_{13.5}\text{Si}_{3.5}\text{C}_2$ *J. Appl. Phys.* **54** 6584–93
- [12] NESSCAP, Co. 2006 Advantages of ultracapacitor versus battery and conventional capacitor http://www.nesscap.com/products_advantages.htm
- [13] IEEE 1991 IEEE standard on magnetostrictive materials: piezomagnetic nomenclature *IEEE STD 319-1990*
- [14] Savage H T and Spano M L 1982 Theory and application of highly magnetoelastic Metglas 2605SC *J. Appl. Phys.* **53** 8092–7
- [15] Engdahl G 2000 *Handbook of Giant Magnetostrictive Materials* (San Diego, CA: Academic)
- [16] Inman D J 2001 *Engineering Vibration* (Upper Saddle River, NJ: Prentice-Hall)
- [17] Thomson W T and Dahleh M D 1998 *Theory of Vibration With Applications* (Upper Saddle River, NJ: Prentice-Hall)
- [18] duToit N E, Wardle B L and Kim S G 2005 Design considerations for MEMS-scale piezoelectric mechanical vibration energy harvesters *Integr. Ferroelectr.* **71** 121–60
- [19] Pons J L 2005 *Emerging Actuator Technologies: A Micromechatronic Approach* (Chichester: Wiley)
- [20] Roundy S and Wright P K 2004 A piezoelectric vibration based generator for wireless electronics *Smart Mater. Struct.* **13** 1131–42
- [21] Elvin N G, Elvin A A and Spector M 2001 A self-powered mechanical strain energy sensor *Smart Mater. Struct.* **10** 293–9
- [22] Blevins R D 1995 *Formulas For Natural Frequency and Mode Shape* (Malabar, FL: Krieger)
- [23] Bhat B R and Wagner H 1976 Natural frequencies of a uniform cantilever with a tip mass slender in axial direction *J. Sound Vib.* **45** 304–7
- [24] Oguamanam D C D 2003 Free vibration of beams with finite mass rigid tip load and flexural–torsional coupling *Int. J. Mech. Sci.* **45** 963–79
- [25] Howatson A M 1996 *Electrical Circuits and Systems: An Introduction For Engineers and Physical Scientists* (Oxford: Oxford University Press)
- [26] Maxim Integrated Products, Inc. 2000 MAX1795, MAX1796, MAX1797 low-supply current, step-up DC–DC converters with true shutdown <http://www.maxim-ic.com>
- [27] Kruusing A, Leppavuori S and Uusimäki A 1999 Printed solenoid windings for miniature electromagnetic devices *J. Micromech. Microeng.* **9** 166–9
- [28] Liu L and Yuan F G 2008 Wireless sensors with dual-controller architecture for active diagnosis in structural health monitoring *Smart Mater. Struct.* **17** 025016